INTERNATIONAL JOURNAL FOR NUMERICAL METHODS IN FLUIDS, VOL. 15, 895–923 (1991)

ANALYSIS OF FLUID FLOW IN CONSTRICTED TUBES AND DUCTS USING BODY-FITTED NON-STAGGERED GRIDS

M. C. MELAAEN

Division of Theromodynamics and Thermal Energy, Norwegian Institute of Technology, N-7034 Trondheim, Norway

SUMMARY

A finite volume method for the calculation of laminar and turbulent fluid flows inside constricted tubes and ducts is described. The selected finite volume method is based on curvilinear non-orthogonal co-ordinates (body-fitted co-ordinates) and a non-staggered grid arrangement. The grids are either generated by transfinite interpolation or an elliptic grid generator. The method is employed for calculation of laminar flows through a tube, a converging–diverging duct and different constricted tubes by both a two- and a three-dimensional computer program. In addition, turbulent flow through an axisymmetric constricted tube is calculated. Both the power law scheme and the second-order upwind scheme are used. The calculated results are compared with the experimental data and with other numerical solutions.

KEY WORDS Constrictions Curvilinear Non-staggered Finite volume

INTRODUCTION

Laminar and turbulent flows inside constricted tubes and ducts are encountered in many engineering situations. The constrictions have often complex geometry, and it is not possible to describe them directly by regular grids (e.g. Cartesian or cylindrical) when using a finite volume method. Even if the blocking-off technique[1] can be used together with regular girds, it is more accurate to use curvilinear non-orthogonal co-ordinates (body-fitted co-ordinates) when describing complex geometries. An alternative to curvilinear non-orthogonal co-ordinates is curvilinear orthogonal co-ordinates. However, the orthogonal co-ordinates have grid lines which are normal to each other, and then the flexibility in the grid line distribution is much less than if curvilinear non-orthogonal grids are used. In addition, there exist constrictions where it is not possible to generate an orthogonal grid. When using curvilinear non-orthogonal co-ordinates, it is possible to use either staggered or non-staggered grid arrangements. From earlier comparisons of these grid arrangements for two-dimensional flows,[2–4] the non-staggered grid arrangement is selected since it is the simplest, uses the least memory and computational time, and the accuracy and the convergence rate are good. In this non-staggered method, the Cartesian velocity components are selected as dependent variables in the momentum equations. The Rhie and Chow interpolation method is used for predicting the convective velocities on the cell faces, and this interpolation method is used together with the SIMPLE (Semi-Implicit Method for Pressure-Linked Equations) algorithm.[5–7] The results of the numerical calculations depend strongly on the differencing scheme selected for the convective terms. In the present paper, the power law scheme[1] and the second-order upwind scheme[6] are selected. At high Reynolds numbers the power law scheme is first-order accurate, while the second-order upwind scheme is second-order accurate. The grids

0271–2091/92/200895–29$19.50

Received September 1991
Revised May 1992

are generated by both transfinite interpolation and an elliptic grid generator.[8] First, the different parts of the grid are generated by transfinite interpolation. Then, the elliptic grid generator is used on the parts of the grid which need remeshing or smoothing.

The objective of this study is to describe an efficient method for calculation of laminar and turbulent incompressible fluid flows inside constricted tubes and ducts. In an attempt to validate the numerical model, the calculated results are compared with the experimental data and with other numerical solutions. The calculations show the desirable properties of curvilinear non-orthogonal co-ordinates when modelling flows inside complex geometries. The flow situations analysed are laminar flow in a tube, laminar flow in a converging–diverging duct, and laminar and turbulent flows in different constricted tubes. These flows are studied by both a two- and a three-dimensional computer program.

First, the mathematical model is given. Co-ordinate transformations and discretization are shown before describing the non-staggered calculation method and the solution algorithm. The selected grid generation methods are presented prior to the calculations, discussion and conclusions.

MATHEMATICAL MODEL

The continuity and momentum equations for steady laminar flow expressed in Cartesian tensor notation are

$$\frac{\partial}{\partial x_i}(\rho u_i)=0 \tag{1}$$

and

$$\frac{\partial}{\partial x_i}(\rho u_i u_k)=\frac{\partial}{\partial x_i}\left(\mu\frac{\partial u_k}{\partial x_i}\right)-\frac{\partial p}{\partial x_k}. \tag{2}$$

When calculating turbulent flows, the k–ε turbulence model with wall functions is selected.[2] The momentum equation then has some more terms.

CO-ORDINATE TRANSFORMATIONS

In Figure 1, a general control volume given by curvilinear non-orthogonal co-ordinates, $(\xi^i)=(\xi, \eta, \zeta)$, is shown. Between the curvilinear and Cartesian co-ordinates there exists a one-to-one mapping. The transformation from Cartesian to curvilinear non-orthogonal co-ordinates is simplified by tensor calculus; some definitions and relations follow.

Two distinct frames of basis vectors exist at any point in a curvilinear non-orthogonal co-ordinate system. One frame follows the co-ordinate lines, while in the other frame, the basis vectors are normal to the co-ordinate surface[7]

$$\mathbf{e}_{(i)}=\frac{\partial x^k}{\partial \xi^i}\,\mathbf{i}_k=J_i^k\,\mathbf{i}_k, \qquad \mathbf{e}^{(i)}=\frac{\partial \xi^i}{\partial x^k}\,\mathbf{i}_k=\bar{J}_k^i\,\mathbf{i}_k. \tag{3}$$

These two vectors are called covariant and contravariant basis vectors, respectively, and are parallel if and only if the co-ordinate transformation is orthogonal.

The chain rule is used when transforming the integrated conservation equations from Cartesian to curvilinear co-ordinates, viz.,

$$\frac{\partial \varphi}{\partial x^i}=\frac{\partial \xi^j}{\partial x^i}\frac{\partial \varphi}{\partial \xi^j}=\bar{J}_i^j\frac{\partial \varphi}{\partial \xi^j}. \tag{4}$$

Next, the face area of a control volume generated by two of the three vectors $\mathbf{e}_{(1)}$, $\mathbf{e}_{(2)}$ and $\mathbf{e}_{(3)}$ is given by

$$\mathbf{A}^{(k)} = A_j^k \, \mathbf{i}_j = \mathbf{e}_{(l)} \times \mathbf{e}_{(m)}, \tag{5}$$

where k, l and m are cyclic. The Jacobian determinant of the co-ordinate transformation is defined by

$$J = \det J_j^i = \mathbf{e}_{(1)} \cdot (\mathbf{e}_{(2)} \times \mathbf{e}_{(3)}). \tag{6}$$

By combination of equations (5), (6) and $\mathbf{e}^{(i)} \cdot \mathbf{e}_{(j)} = \delta_j^i$, $\bar{J}_k^i$ is obtained:

$$\bar{J}_k^i = A_k^i / J. \tag{7}$$

If the control volume has the dimensions $(\delta\xi, \delta\eta, \delta\zeta)$ in the computational space, the corresponding area and volume in physical space are

$$\delta\mathbf{A}^{(k)} = \mathbf{A}^{(k)} \, \delta\xi^l \, \delta\xi^m, \qquad \delta V = J \, \delta\xi \, \delta\eta \, \delta\zeta, \tag{8}$$

respectively, where k, l and m are cyclic. The choice of the values of $\delta\xi^i$ is free, the value selected here being unity.

DISCRETIZATION

The continuity and momentum equations can be treated partly as scalar equations and, therefore, it is desirable first to discretize a general scalar equation in which φ is the scalar dependent variable. A general co-ordinate-invariant, strong-conservation form of the governing equation is

$$\nabla \cdot \mathbf{J} = S, \tag{9}$$

where

$$\mathbf{J} = \rho \mathbf{U} \varphi - \Gamma \nabla \varphi. \tag{10}$$

Here φ, Γ and S are redefined for the different conservation equations that are solved.

Since the finite volume concept is employed, the co-ordinate invariant equation is integrated over a general control volume, δV, around grid point P in physical space (Figure 1) and then the divergence theorem is used:

$$\mathbf{J} \cdot \mathbf{A}^{(1)}|_e - \mathbf{J} \cdot \mathbf{A}^{(1)}|_w + \mathbf{J} \cdot \mathbf{A}^{(2)}|_n - \mathbf{J} \cdot \mathbf{A}^{(2)}|_s + \mathbf{J} \cdot \mathbf{A}^{(3)}|_t - \mathbf{J} \cdot \mathbf{A}^{(3)}|_b = \bar{S}_P, \tag{11}$$

where the subscripts e, w, n, s, t and b indicate the different faces of the control volume.

The co-ordinate transformations produce

$$\mathbf{J} \cdot \mathbf{A}^{(i)}|_{nn} = \left(\rho \hat{U}^i \varphi - \Gamma G^{ij} \frac{\partial \varphi}{\partial \xi^j} \right)_{nn} = \hat{J}_{nn}^i, \tag{12}$$

and

$$\hat{U}^i = u_j A_j^i = \mathbf{U} \cdot \mathbf{A}^{(i)}, \qquad G^{ij} = \frac{A_k^i A_k^j}{J} = \frac{\mathbf{A}^{(i)} \cdot \mathbf{A}^{(j)}}{J}, \tag{13}$$

and the linearized source term can be written as

$$\bar{S}_P = \int_{\delta V} S \, \mathrm{d}V = \bar{S}_{1P} + \bar{S}_{2P} \, \varphi_P. \tag{14}$$

When the co-ordinate system is orthogonal, G^{ij} is zero for $i \neq j$. Then the total flux through

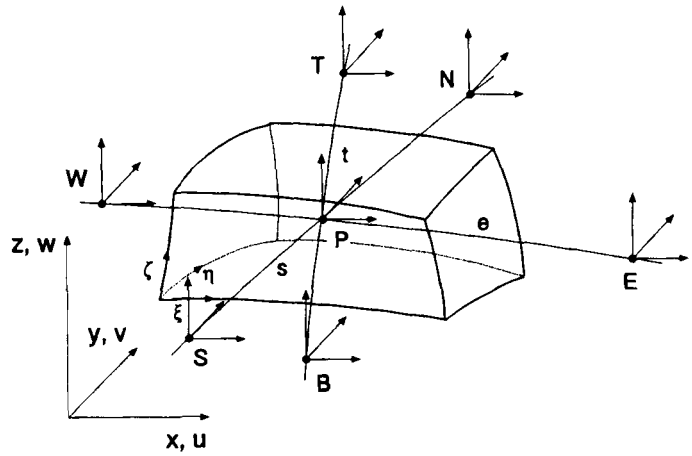

Figure 1. Curvilinear non-staggered grid arrangement

a given face is divided into orthogonal and non-orthogonal parts, $\hat{J}^i_O$ and $\hat{J}^i_{NO}$, viz.,

$$\hat{J}^i_{nn}=(\hat{J}^i_O)_{nn}+(\hat{J}^i_{NO})_{nn}, \tag{15}$$

where

$$\hat{J}^i_O=\rho\hat{U}^i\varphi-\Gamma G^{ii}\frac{\partial\varphi}{\partial\xi^i}, \qquad \hat{J}^i_{NO}=-\left(\Gamma G^{ij}\frac{\partial\varphi}{\partial\xi^j}\right)_{i\neq j}. \tag{16}$$

The orthogonal flux $(\hat{J}^i_O)_{nn}$ is discretized in the same manner as on regular grids (e.g. Cartesian), for instance by the power law scheme (POW) or the second-order upwind scheme (SOU). Following the methodology of Patankar,[1] the orthogonal flux for the power law scheme can be written as

$$(\hat{J}^1_O)_e=A(P^1_e)D^1_e(\varphi_P-\varphi_E)+F^1_e\varphi_P, \tag{17}$$

$$(\hat{J}^1_O)_w=A(-P^1_w)D^1_w(\varphi_W-\varphi_P)+F^1_w\varphi_P, \tag{18}$$

where

$$A(P^i)=|[0,(1-0{\cdot}1|P^i|)^5]|+|[0,-P^i]| \tag{19}$$

and

$$P^i_{nn}=\frac{F^i_{nn}}{D^i_{nn}}, \qquad F^i_{nn}=(\rho\hat{U}^i)_{nn}, \qquad D^i_{nn}=\left(\frac{\Gamma G^{ii}}{\delta\xi^i}\right)_{nn}. \tag{20}$$

Here $|[\ ]|$ means the largest of the expressions contained within it.

When the second-order upwind scheme[6] is selected, the convected variable on the cell face is given by a linear extrapolation from the two upstream neighbouring nodes:

$$\varphi_e=\begin{cases}\varphi_E+(\varphi_E-\varphi_{EE})f_{1E}, & F^1_e<0\\ \varphi_P+(\varphi_P-\varphi_W)(1-f_{1W}), & F^1_e>0,\end{cases} \tag{21}$$

where the physical weighting interpolation factor is

$$f_{1P}=\frac{\overline{Pe}}{\overline{PE}}, \tag{22}$$

and point EE is east of point E.

For the diffusive terms in the orthogonal flux (when using the second-order upwind scheme) and the non-orthogonal diffusive terms, a linear variation of the dependent variables, together with central differencing, is used. If the non-orthogonal terms are discretized implicitly, both positive and negative coefficients appear. However, when an iterative method is used for the solution of the discretized equations, it is preferable to work with positive coefficients, since negative coefficients may produce numerical instability and unrealistic solutions. To achieve this, the non-orthogonal flux $(\hat{J}^i_{NO})_{nn}$ is lumped into the source term, and then the non-orthogonal part of the equations is treated explicitly. Here $\bar{S}_{2P}$ has to be selected negative to ensure a numerically stable solution. The final equations to be solved have the form

$$a_P\varphi_P=\sum_{nb} a_{nb}\varphi_{nb}+b, \tag{23}$$

where nb indicates summation over neighbouring gird points and

$$a_P=\sum_{nb} a_{nb}-\bar{S}_{2P}, \qquad b=b_{NO}+\bar{S}_{1P}, \tag{24}$$

where

$$b_{NO}=\left[\Gamma G^{12}\frac{\partial\varphi}{\partial\xi^2}+\Gamma G^{13}\frac{\partial\varphi}{\partial\xi^3}\right]^e_w+\left[\Gamma G^{21}\frac{\partial\varphi}{\partial\xi^1}+\Gamma G^{23}\frac{\partial\varphi}{\partial\xi^3}\right]^n_s+\left[\Gamma G^{31}\frac{\partial\varphi}{\partial\xi^1}+\Gamma G^{32}\frac{\partial\varphi}{\partial\xi^2}\right]^t_b \tag{25}$$

and the coefficients in the ξ-direction for the power law scheme are

$$a_E=D^1_e A(P^1_e), \qquad a_W=D^1_w A(-P^1_w), \tag{26}$$

while the coefficients in the ξ-direction for the second-order upwind scheme are

$$a_E=|[0, -F^1_e]|(1+f_{1E})+|[0, -F^1_w]|f_{1P}+D^1_e, \tag{27}$$

$$a_W=|[0, F^1_w]|(2-f_{1WW})+|[0, F^1_e]|(1-f_{1W})+D^1_w, \tag{28}$$

$$a_{EE}=-|[0, -F^1_e]|f_{1E}, \tag{29}$$

$$a_{WW}=-|[0, -F^1_w]|(1-f_{1WW}), \tag{30}$$

with similar a_{nb} coefficients in η- and ζ-direction.

From Taylor series analysis, the second-order upwind scheme is second-order accurate whereas the power law scheme is first-order accurate at high Reynolds numbers; hence, the power law scheme produces most false diffusion when the grid lines and streamlines do not follow each other. Unfortunately, the second-order scheme does not generally produce a bounded solution. This occurs because the coefficients of the most distant nodes EE, WW, NN, SS, TT and BB can be negative. Since an iterative method may produce numerical divergence for negative coefficients, the negative coefficients of the most distant nodes are incorporated into the source and treated explicitly to deduce a more robust algorithm. In the source term, this addition arises for

the second-order upwind scheme:

$$\Delta b = a_{EE}(\varphi_{EE} - \varphi_P) + a_{WW}(\varphi_{WW} - \varphi_P) + a_{NN}(\varphi_{NN} - \varphi_P) + a_{SS}(\varphi_{SS} - \varphi_P) + a_{TT}(\varphi_{TT} - \varphi_P) + a_{BB}(\varphi_{BB} - \varphi_P). \tag{31}$$

This requires nb in equation (23) to equal E, W, N, S, T and B. Then, all coefficients in SOU are positive during the iterations. This has been found to improve the stability and the convergence rate.

Since the main part of the laminar momentum equations based on Cartesian velocity components can be treated similar to the general scalar equation ($\varphi = u_k$), it is only the pressure term which, in addition, needs integration:

$$\int_{\delta V} -\frac{\partial p}{\partial x^k}\,\mathrm{d}V = -\left(A_k^j \frac{\partial p}{\partial \xi^j}\right)_P. \tag{32}$$

Although the above integration is based on a three-dimensional flow, only small changes are needed for axisymmetric flow; the radius appears in the conservation equations, and a simple additional term appears in the radial momentum equation. The strategy followed above is also followed for turbulent flow. The additional terms in the momentum equations are integrated over the control volume, and the same is done for the source terms in the scalar k- and ε-equations. In addition, the wall functions need special treatment since curvilinear non-orthogonal co-ordinates are used.

NON-STAGGERED CALCULATION

For the non-staggered grid arrangement, the Cartesian velocity components are stored in scalar grid points (Figure 1) and then velocity interpolation is needed when the convective flux at the control volume faces must be estimated. The straightforward linear interpolation between two velocity components leads to chequerboard oscillations in pressure and velocity.[1] The reason is the $2\delta\xi^i$-differences of velocity and pressure gradients, which is insensitive to $1\delta\xi^i$-variations; the even and odd grid points are decoupled. If a non-staggered calculation is to be successful, a close coupling between pressure and convective velocity is required. This is achieved by the Rhie and Chow interpolation method:[5,7]

$$\hat{U}_e^i = \bar{\hat{U}}_e^i + \bar{C}_e^{ii}\left[\left(\overline{\frac{\partial p}{\partial \xi^i}}\right)_e - \left(\frac{\partial p}{\partial \xi^i}\right)_e\right] \tag{33}$$

where

$$\bar{C}^{ii} = A_k^i A_k^i \left(\overline{\frac{1}{a_P}}\right). \tag{34}$$

The overbar means weighted linear interpolation from neighbouring grid points. To find a solution independent of under-relaxation, the under-relaxation factor is not included in a_P.

SOLUTION ALGORITHM

The coupling between the pressure and velocity fields is handled by using the SIMPLE algorithm.[1] A pressure-correction equation with the same form as equation (23) can be deduced. This pressure-correction equation contains non-orthogonal terms. Since the pressure correction goes

to zero for a converged solution, it is possible to neglect the non-orthogonal terms, and then only a seven-point computational molecule, with only positive coefficients, appears when solving the pressure-correction equation. The solution algorithm is then: solve the momentum equations, find the tentative $\hat{U}^i$ from the Rhie and Chow interpolation formula, solve the pressure-correction equation, correct the pressure, mass flow rate and Cartesian velocity components, and solve scalar equations if necessary. The equations are solved by line-by-line TDMA together with block correction.[2] The process is repeated until convergence is obtained. The solution algorithm is incorporated into a two- and three-dimensional computer program system.

GRID GENERATION

Transfinite interpolation

The transfinite interpolation method is an algebraic grid generator. Different transfinite interpolation methods exist, but here a method discussed by Thompson *et al.*[8] has been adopted

$$\mathbf{r}(\xi,\eta)=\sum_{n=1}^{2}\phi_n\left(\frac{\xi}{I}\right)\mathbf{r}(\xi_n,\eta)+\sum_{m=1}^{2}\psi_m\left(\frac{\eta}{J}\right)\mathbf{r}(\xi,\eta_m)-\sum_{n=1}^{2}\sum_{m=1}^{2}\phi_n\left(\frac{\xi}{I}\right)\psi_m\left(\frac{\eta}{J}\right)\mathbf{r}(\xi_n,\eta_m). \quad (35)$$

This equation distributes grid points inside the domain, if the grid points on the boundary are known. The blending functions in equation (35) are any functions which satisfy the conditions

$$\phi_n\left(\frac{\xi_l}{I}\right)=\delta_n^l, \qquad n=1,2, \quad l=1,2, \quad (36)$$

$$\psi_m\left(\frac{\eta_l}{J}\right)=\delta_m^l, \qquad m=1,2, \quad l=1,2, \quad (37)$$

such as the linear functions

$$\phi_1\left(\frac{\xi}{I}\right)=1-\frac{\xi}{I}, \quad (38)$$

$$\phi_2\left(\frac{\xi}{I}\right)=\frac{\xi}{I}. \quad (39)$$

Equation (35) can be used on a general curved surface in three-dimensional space, because it gives the component equations for x, y and z. These values appear directly after specifying ξ and η; hence, the method is non-iterative with a low computational time. The equation can be used in a two-dimensional plane by setting one Cartesian co-ordinate constant, or in three dimensions by generating subsequent curved sufaces.

Elliptic grid generator

Since the transfinite interpolation method used in this study does not produce a smooth grid, it is often desirable and even necessary to smooth the algebraic grid by an elliptic grid generator. To generate an elliptic grid, a system of differential equations has to be solved:[8]

$$\nabla^2\xi^i=P^i, \quad i=1,2,3. \quad (40)$$

Lines of constant ξ^i are used to describe the grid lines. Then it is much more convenient to transform equation (40) in such a way that the dependent and independent variables are

interchanged. The final equations can be solved numerically for the Cartesian co-ordinates x^i on an equally spaced grid in the computational domain. A simple way to transform equation (40) is by writing

$$\nabla^2 \mathbf{r} = 0 \tag{41}$$

This equation is rewritten using equation (4),

$$\nabla^2 \xi^l = \bar{J}^j_k \frac{\partial}{\partial \xi^j} (\bar{J}^l_k),$$

and equation (40). The result is

$$g^{ij} \frac{\partial^2 \mathbf{r}}{\partial \xi^i \partial \xi^j} + P^j \frac{\partial \mathbf{r}}{\partial \xi^j} = 0, \tag{42}$$

where $g^{ij} = \mathbf{e}^{(i)} \cdot \mathbf{e}^{(j)}$. Both the first and the second derivatives are found by central differencing.

The spacing of the grid lines, smoothness and non-orthogonality can be affected by adjusting the values of the source terms $P^i = (P, Q, R)$ in equation (42). Different possible sources exist. For instance, series of exponential functions as the source terms are often used;[8,9] they are also used in the present work. These functions are:

$$P(\xi, \eta, \zeta) = -\sum_{l=1}^{m} a_{l_1} \operatorname{sgn}(\xi - \xi_l) \exp(-b_{l_1} T_l), \tag{43}$$

$$Q(\xi, \eta, \zeta) = -\sum_{l=1}^{m} a_{l_2} \operatorname{sgn}(\eta - \eta_l) \exp(-b_{l_2} T_l), \tag{44}$$

$$R(\xi, \eta, \zeta) = -\sum_{l=1}^{m} a_{l_3} \operatorname{sgn}(\zeta - \zeta_l) \exp(-b_{l_3} T_l), \tag{45}$$

where

$$T_l = \sqrt{c_{l_1}(\xi - \xi_l)^2 + c_{l_2}(\eta - \eta_l)^2 + c_{l_3}(\zeta - \zeta_l)^2}. \tag{46}$$

The value of the coefficients a_{l_n} and c_{l_n} are used to decide whether the planes ξ, η and/or ζ = constant are attracted to a specified plane, co-ordinate line or grid point. The strength of the attraction is controlled by the decay factor, b_{l_n}. If ξ-planes are attracted, the a_{l_1} have to be different from zero. Correspondingly, the a_{l_2} and a_{l_3} are different from zero when the η- and ζ-plane are attracted.

The point successive over-relaxation (SOR) method is used for solving the equations describing the grid. After the grid is generated, all geometric information necessary in the discretized conservation equations is calculated from equations (5), (6) and (8).

RESULTS AND DISCUSSION

Laminar flow in a converging–diverging duct

Maliska and Raithby[10] have predicted laminar flow through a converging–diverging duct (Figure 2). They used a parabolic program based on non-orthogonal co-ordinates. A rectangular inlet section with an aspect ratio of 3 changes gradually into a circular outlet. This duct exhibits strong convergence in the vertical direction, and mild divergence in the horizontal direction. The strong convergence in the vertical direction creates a secondary flow in the same direction, and

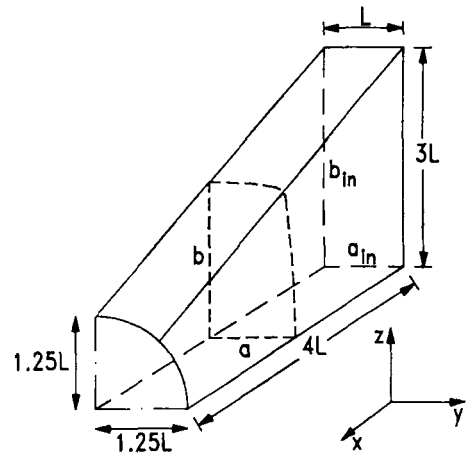

Figure 2. One quarter of the converging–diverging duct

with the same order of magnitude as the principal flow in the x-direction. Due to symmetry, only one quarter of the channel has to be calculated. Then two of the boundaries are symmetry planes.

Since the cross-section of the duct changes from a rectangle to a circle, neither Cartesian nor cylindrical co-ordinates are usable. Curvilinear non-orthogonal co-ordinates are needed. It seems natural to start with Cartesian co-ordinates at the inlet, and then gradually deform that grid until the circle at the outlet is described. The grid at the circular outlet is then strongly non-orthogonal.

However, before the duct is calculated, the effect of such a highly distorted grid is analysed. This is done by calculating one quarter of a fully developed tube flow by the three-dimensional program. Normal to the flow direction, the elliptic generated grid shown in Figure 3(a) is used.

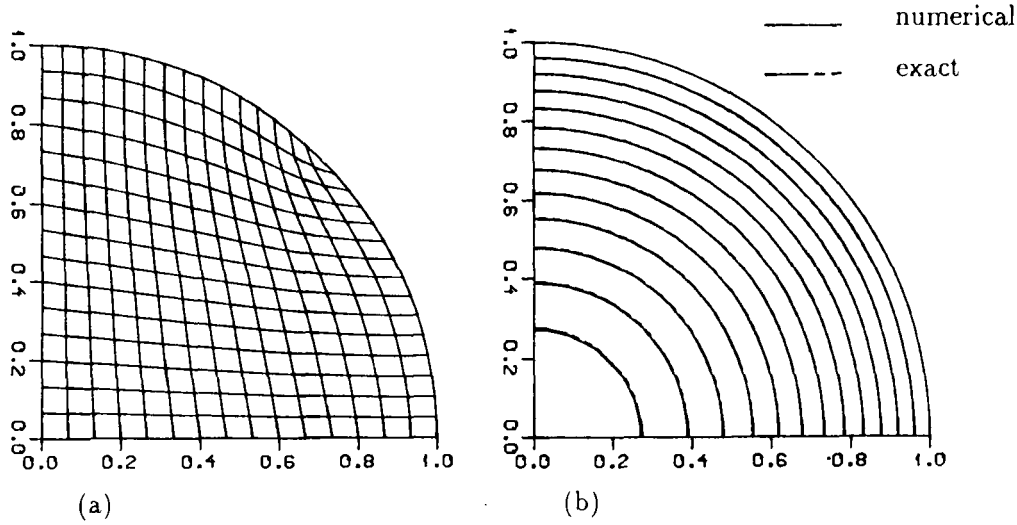

Figure 3. (a) Grid normal to the tube flow, 17 × 17. (b) Isolines of the fully developed axial velocity, $u/2\bar{U}$. The isolines are uniformly distributed from 0 to 1

Three control volumes are selected in the flow direction. The velocity profile at the inlet is given by the outlet velocity. At convergence, the fully developed tube flow appears. For fully developed laminar tube flow an analytical solution for the velocity and the friction coefficient, C_f, exist:

$$u=2\bar{U}\left[1-\left(\frac{r}{r_0}\right)^2\right], \qquad C_f Re=16, \tag{47}$$

where

$$C_f=\frac{2\tau_w}{\bar{U}^2\rho}, \quad Re=\frac{\bar{U}D}{\nu} \tag{48}$$

and $\bar{U}$ is the mean tube velocity and τ_w the wall shear stress.

In Figure 3(b), the calculated u-velocity is compared with the exact solution. The agreement is good, also near the highly deformed grid corner. In Table I, the calculated friction coefficients are given. The calculated and analytical solutions are in close agreement. The table also lists the friction coefficient calculated by the two-dimensional program. Seventeen grid points were uniformly distributed in the radial direction. It is seen that the three-dimensional program gives a better solution than the two-dimensional program. This is due to the grid point distribution in the radial direction. The grid points on the boundary of the three-dimensional grid (Figure 3(a)) are uniformly distributed. However, in the inside domain, the grid points are closer to the wall than in the two-dimensional grid, and even if the grid is highly distorted, this three-dimensional calculation resolves the steep gradients better.

From this initial calculation it is seen that even though the grid is highly distorted, the results are good; hence, similar grids can be used to calculate the converging–diverging duct and also analogous problems.

Maliska and Raithby[10] describe the contours of the duct cross-sections by

$$\left(\frac{y}{a}\right)^m+\left(\frac{z}{b}\right)^m=1, \tag{49}$$

where a and b are the half-duct dimensions in the y- and z-direction, respectively (Figure 2). If $m\to\infty$, a rectangular duct is obtained, while $m=2$ and $a=b$ give a circular duct. In the x-direction, an equal spacing of eight control volumes has been used. Table II gives the staggered positions and the constants describing the geometry.[10] The hydraulic diameter at the inlet, D_h, is equal to $3L$.

A grid point density of $10\times17\times17$, equal to the one used by Maliska and Raithby[10] is selected. Each grid in the plane normal to the x-axis is generated by the elliptic grid generator, where the source terms Q and R are used (Figure 4).

The continuity and momentum equations are non-dimensionalized with the length scale D_h ($X=x/D_h$) and by the average inlet velocity $\bar{U}$ ($U=u/\bar{U}$). The flow studied has a Reynolds number, $\bar{U}D_h/\nu$, of 1000. A predicted fully developed velocity profile for a rectangular duct is prescribed as the inflow boundary condition. Usual symmetry and wall boundary conditions are

Table I. Analytical and predicted friction coefficients

	Analytical	Two-dimensional	Three-dimensional
$C_f Re$	16	15·9292	15·9584

Table II. Constants defining the boundary shape of the converging–diverging duct

Plane N	b/a	m	x/D_h
1	3·000	∞	0
2	2·696	18·58	1/6
3	2·411	9·115	2/6
4	2·142	5·957	3/6
5	1·888	4·377	4/6
6	1·648	3·428	5/6
7	1·421	2·794	6/6
8	1·205	2·340	7/6
9	1·000	2·0	8/6

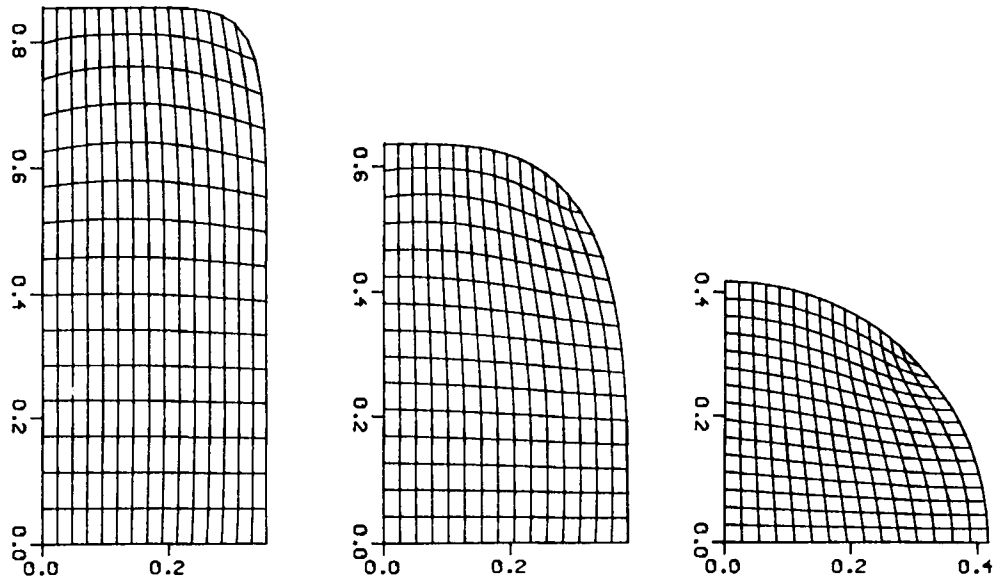

plane 3 plane 6 plane 9

Figure 4. Grid used to calculate the converging–diverging duct

incorporated. A linear extrapolation estimates the velocity components at the outlet, but in addition the u-component is forced to satisfy global continuity.

The pressure averaged over the plane normal to the x-axis is shown in Figure 5. The SOU produces results in better accordance with the calculation of Maliska and Raithby[10] than the POW. Even if Maliska and Raithby[10] use a parabolic program, the agreement is quite good, except for the outlet. The deviation probably occurs because the present elliptic program requires an outlet boundary condition, whereas the parabolic program does not. In addition, if the present grid is finer by the wall, the steep gradients are better resolved and the pressure drop increases. Figure 6 shows the isobars in the planes $Y=0$ and $Z=0$.

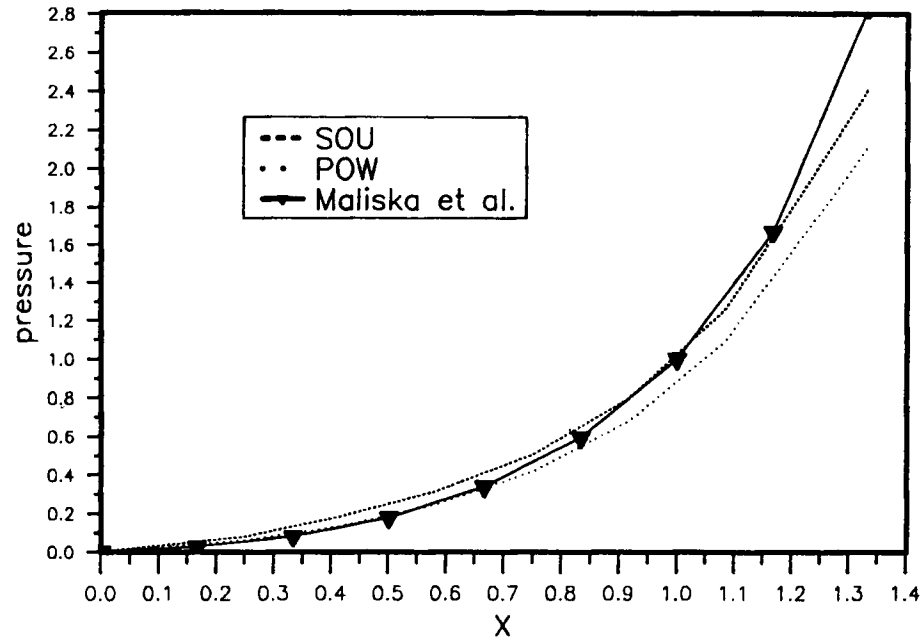

Figure 5. Average pressure drop, $(\bar{p}_{in}-\bar{p})/\rho\bar{U}^2$

The U-velocity profiles in the planes $Y=0$ and $Z=0$ are shown in Figures 7 and 8. The deviation between POW and SOU is small. The strong contraction of the duct in the Z-direction produces a strong acceleration of the flow core, which causes the U-velocity profiles to be flatter in the $Y=0$ plane. In the $Z=0$ plane, it is seen that the slight expansion results in an inflection in the profiles. The inflection point appears because the flow has to fill the space created by the divergence of the duct. Due to the strong vertical contraction, significant secondary flow is induced (Figure 9). This cross flow has a stagnation point in the $Z=0$ plane because of the duct divergence in the Y-direction. The same fundamental flow profiles were reported by Maliska and Raithby.[10]

If the normalized norm of the residuals are less than 10^{-3} for all equations, the solution is said to have converged. The necessary number of iterations for POW is 39 and for SOU 43. When the block-correction method is omitted and only TDMA used, POW needed 133% more iterations; this indicates the power of the block-correction method.

Laminar flow through constricted tubes

Young and Tsai[11] studied the flow in non-axisymmetric constrictions experimentally (Figure 10). Three-dimensional complex flows appear through these constrictions, which were formed by inserting a cylindrical section through the wall of the tube. The radius of the constriction, R_c, and the height, δ, may be varied to give different flow situations. In Table III, the geometrical characteristics corresponding to models M4 and M5 of Young and Tsai are shown. Young and Tsai[11] have measured the critical Reynolds number which gives transition from laminar to turbulent flow. In the present work, Reynolds numbers well within the laminar region were selected.

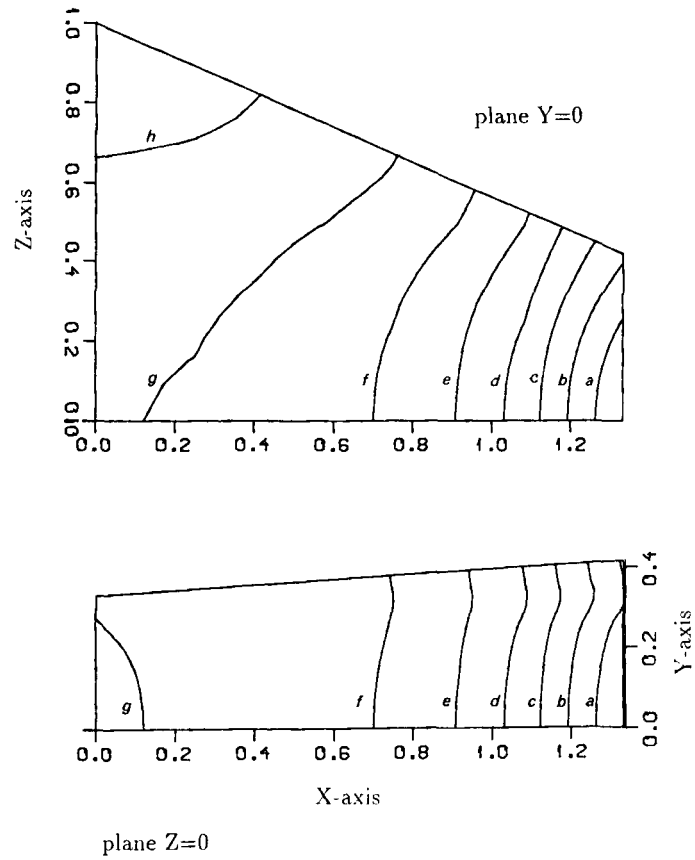

Figure 6. Isobars, $p/\rho\bar{U}^2$, calculated by SOU

The continuity and momentum equations are made non-dimensional by the length scale R_0 and the velocity scale $2\bar{U}$. At the inlet, a fully developed laminar flow is prescribed. Due to symmetry, only half the flow is calculated. Usual wall boundary conditions are selected and zero gradients are assumed at the outlet. The calculations start at the non-dimensional position $X = -6$ and end at position 20. The grid is expanded in both directions away from the constriction (Figure 11). In the YZ-plane, the grid is generated by solving a system of Poisson equations. The presented results are calculated on a $72 \times 18 \times 30$ grid. This final grid shows that curvilinear non-orthogonal co-ordinates can accurately model the present complex geometry.

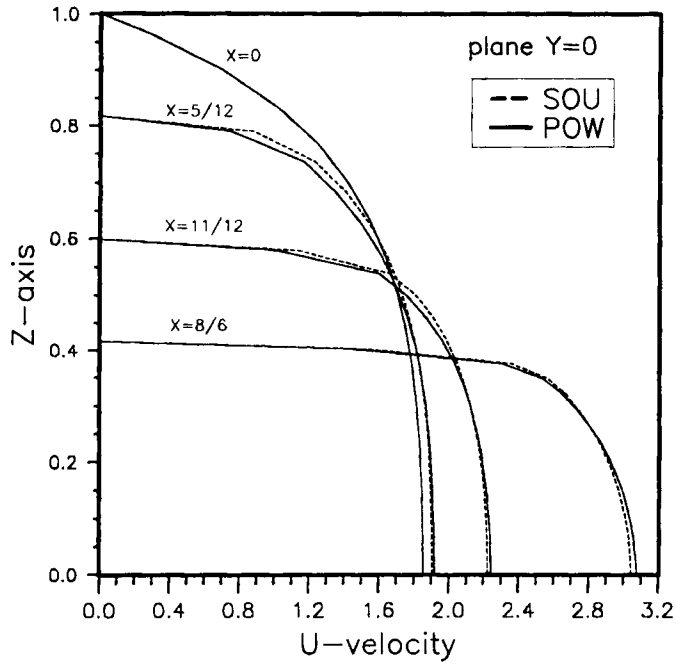

Figure 7. U-velocity profiles in the symmetry plane $Y=0$

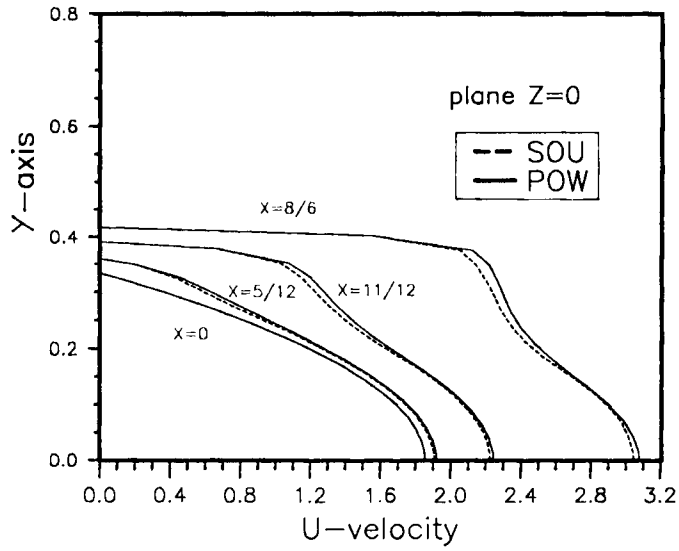

Figure 8. U-velocity profiles in the symmetry plane $Z=0$

First the flow in model M4 is studied. For $Re=200$ and 650, 123 and 172 iterations are needed for POW, while SOU uses about 40% more iterations and computational time for $Re=200$. In Table IV, the calculated separation and reattachment lengths in the symmetry plane are given. The present results are compared with the measurements[11] and the numerical results obtained by

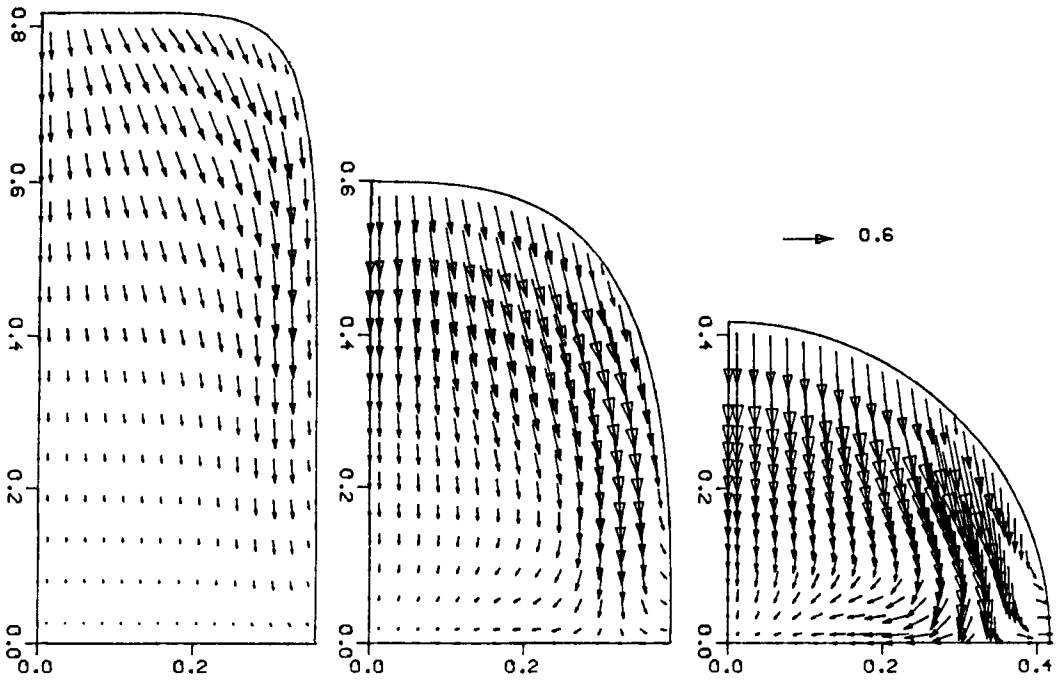

Figure 9. Cross flow velocity at different X-positions, $X = 5/12, 11/12, 8/6$, SOU

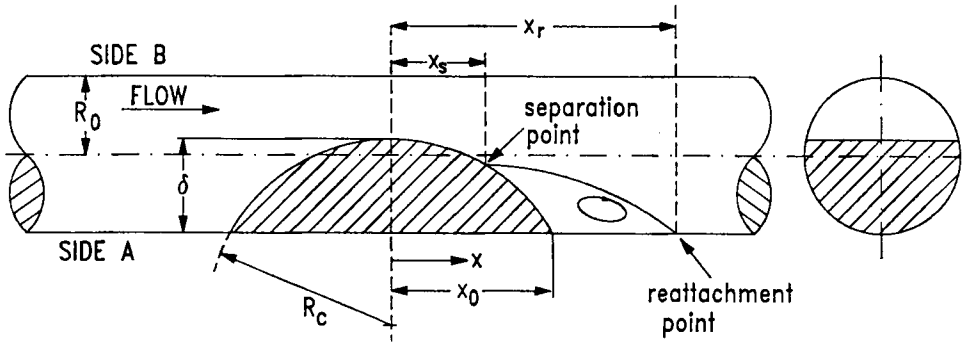

Figure 10. Geometric configuration for the non-axisymmetric constrictions

Table III. Model geometry

Model	R_0 (cm)	δ/R_0	x_0/R_0	R_c/R_0	Percentage reduction in flow area
M4	0·945	1·08871	4	7·90323	56
M5	0·945	1·66667	4	5·64516	89

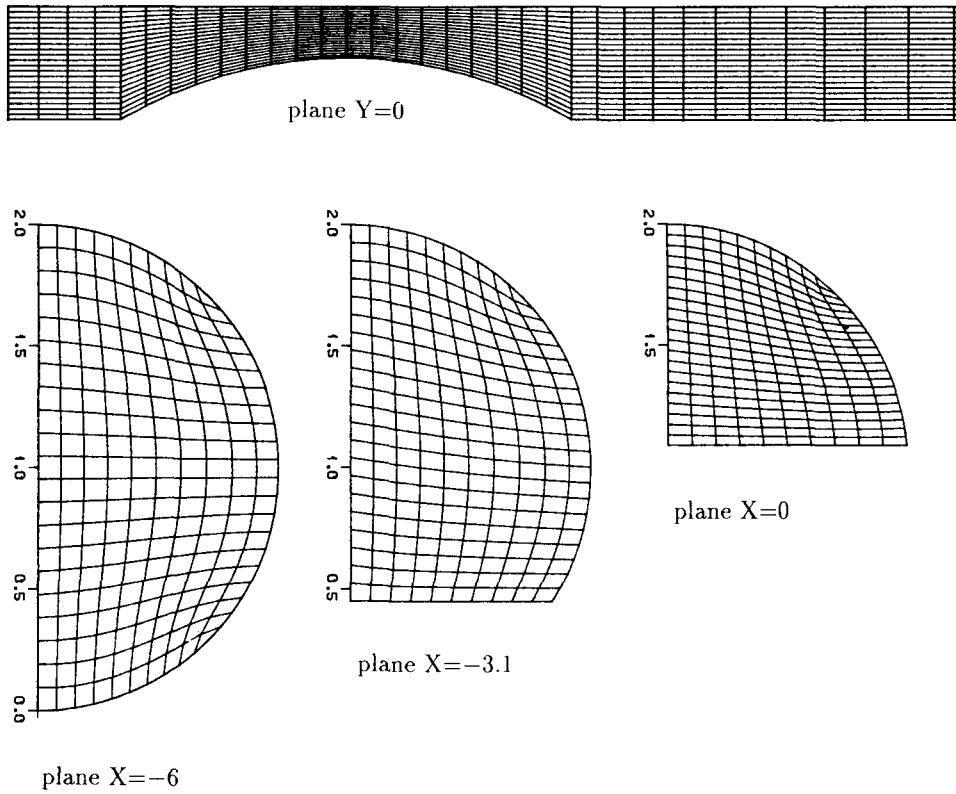

Figure 11. Fundamental grid for model M4

Table IV. Separation and reattachment lengths, model M4

	X_s/X_0			X_r/X_0		
Reynolds number	200	300	650	200	300	650
Experiment, Young	0·77	0·68	0·57	1·40	1·45	2·57
Rastogi, POW	0·72	0·67	0·51	1·41	1·62	2·05
Present, POW	0·78	0·72	0·56	1·49	1·65	1·95
Present, SOU	0·80	0·77	0·70	1·59	1·81	2·21

Rastogi.[12] The measured data have scatter due to the dye-tracing technique used. Rastogi employed a staggered method based on non-orthogonal co-ordinates and POW, and a $100 \times 20 \times 40$ grid was selected. The separation points obtained by the present non-staggered method are always best predicted by POW. The reattachment points at $Re = 200$ and 300 are also best predicted by POW, whereas at $Re = 650$, SOU is closer to the measured reattachment point. The results obtained by Rastogi and the present results from calculation based on POW are in good agreement. SOU gives a too late separation and also a too late reattachment for all but $Re = 650$.

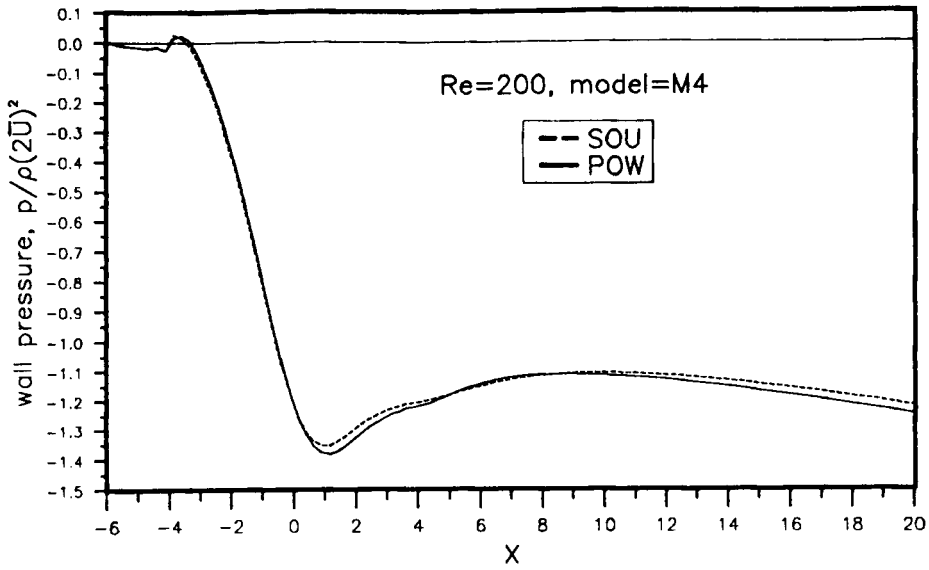

Figure 12. Pressure along the constricted wall in the symmetry plane, model M4, $Re = 200$

Measurements indicate that, as the Reynolds number increases, the separation point tends to the point of minimum cross section and the reattachment point tends to move downstream. Both POW and SOU predict the same trend. Due to the three-dimensional flow, the separation appears along a line on the constriction. Near the tube wall, separation starts earlier than in the symmetry plane. SOU produces a greater deviation between these two points than POW. As the Reynolds number increases, the recirculation zone grows up the tube wall. At $Re = 650$, POW predicts a recirculation zone covering the whole tube circumference, while SOU also nearly gives a recirculation zone around it. However, these zones are thin and the grid is too coarse to describe these zones accurately. In addition to the recirculation after the constriction, a small recirculation bubble appears at the beginning of the constriction for $Re = 300$ and 650.

In Figures 12 and 13, the pressure in the symmetry plane along the wall of the constriction is shown for $Re = 200$ and 650. In front of the constriction, the pressure first increases due to stagnation of the flow. Minimum pressure occurs downstream of the throat of the constriction. The dimensionless pressure drop decreases with increasing Reynolds number. As expected, POW and SOU show best agreement at the lowest Reynolds numbers. POW produces a faster pressure recovery than SOU at $Re = 650$.

Velocities and isobars in the symmetry plane calculated for the flow with $Re = 650$ are shown in Figure 14. The results are achieved primarily by SOU, but, as a comparison, the results obtained by POW are given for the U- and W-velocity profiles. Figure 14(b) gives the U-velocity isolines. This figure also shows the separation and reattachment points. In Figure 15, the cross flow velocity vectors at different X-positions are given.

Flow through model M5 is calculated at $Re = 50$. No separation appears in front of the constriction. The recirculation zone downstream of the constriction covers the whole tube wall circumference. In Table V, the separation and reattachment lengths on the step side A and on the opposite side B are given. Separation starts along a line on the constriction. The values in Table V are valid for the symmetry plane. Compared to measurements, POW and SOU give separation

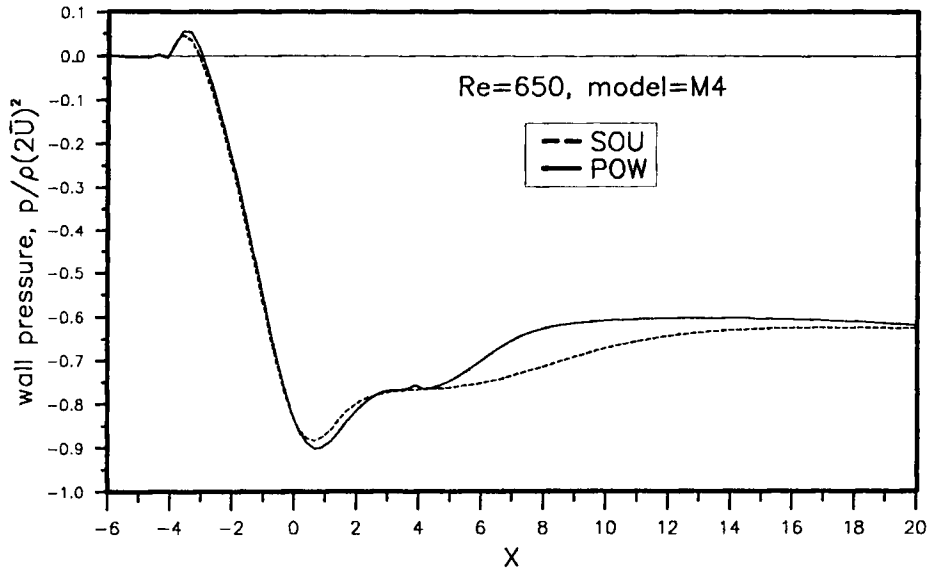

Figure 13. Pressure along the constricted wall in the symmetry plane, model M4, $Re = 650$

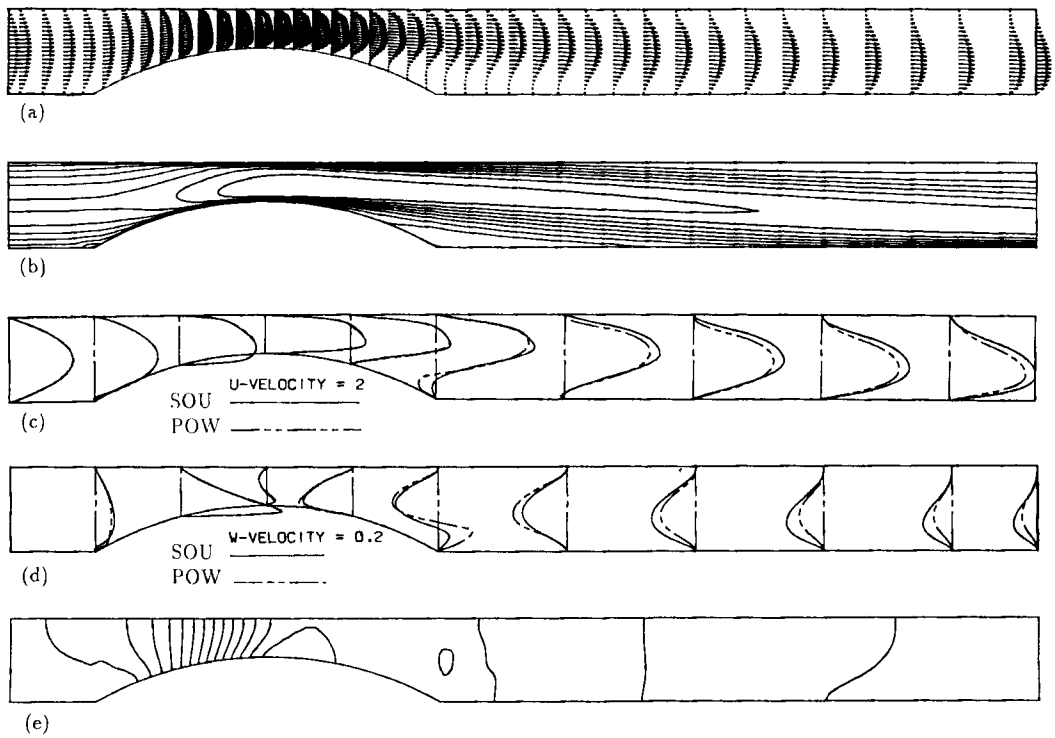

Figure 14. Flow in the symmetry plane at $Re = 650$, model M4: (a) velocity vectors; (b) U-velocity isolines; (c) U-velocity profiles (The length of the lines for the U-velocity is equal to 2, and this gives the scale for the profiles.); (d) W-velocity profiles; (e) isobars. The profiles are in positions $X = -6, -4, -2, 0, 2, 4, 7, 10, 13, 16, 18$

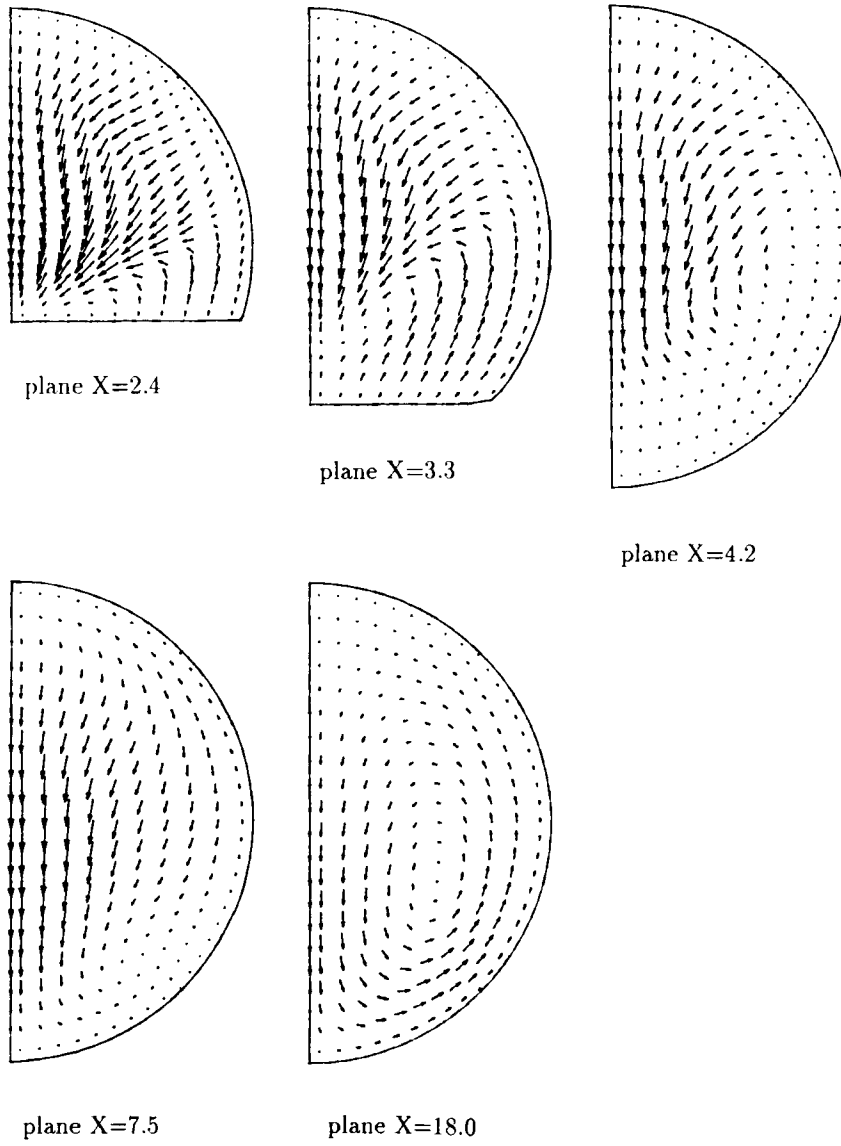

Figure 15. Cross flow velocity vectors calculated by SOU, model M4, $Re=650$

Table V. Separation and reattachment lengths on sides A and B, model M5, $Re=50$

	Side A		Side B	
	X_s/X_0	X_r/X_0	X_s/X_0	X_r/X_0
Experiment Young	0·67	2·60	—	2·10
Present, POW	0·76	2·16	1·99	2·31
Present, SOU	0·77	2·30	1·98	2·67

on side A too far downstream. The reattachment point is best predicted by SOU. On side B, POW and SOU generate separation at the same point. This point was not measured. Both POW and SOU predict a reattachment point too far downstream on side B, but SOU deviates most from the experimental data. While measurements indicate that reattachment appears earlier on side B than on side A, POW and SOU give the opposite result.

In Figure 16, the pressure drop along the wall with the constriction is shown. As a comparison, the pressure drop in an axisymmetric constriction called model M2 is also shown.[2] Both the axisymmetric model M2 and model M5 have an area reduction of 89%. As shown in Figure 16, the non-axisymmetric model M5 produces higher pressure drop than the axisymmetric model M2; in addition, the non-axisymmetric model M5 gives less pressure recovery. POW predicts a higher pressure drop than SOU. In both models the minimum pressure appears downstream of the minimum flow area. These trends were also pointed out by Young.

The velocities and pressures in the symmetry plane calculated by SOU are shown in Figure 17. The isobars indicate little variation of the pressure normal to the X-axis. Due to the low Reynolds number, the flow reaches quickly the fully developed laminar flow profile.

Turbulent flow through an axisymmetric constricted tube

Turbulent flow through an axisymmetric constricted tube (Figure 18) has been studied experimentally by Deshpande and Giddens.[13] The general shape of the axisymmetric constriction is specified as the cosine curve.

$$\frac{R}{R_0}=1-\frac{\delta}{2R_0}\left(1+\cos\frac{\pi x}{x_0}\right), \quad -x_0<x<x_0, \tag{50}$$

where the characteristics of the geometry are given in Table VI. A flow with Reynolds number ($\bar{U}2R_0/\nu$) equal to 15000 is calculated. The computational domain is extended from x-position

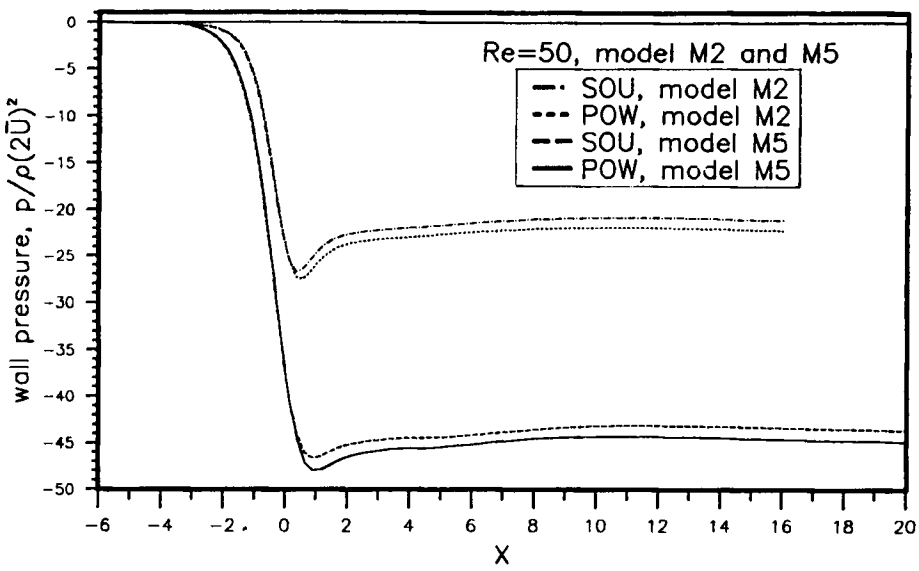

Figure 16. Pressure along the constricted wall for model M5 and axisymmetric model M2, $Re=50$

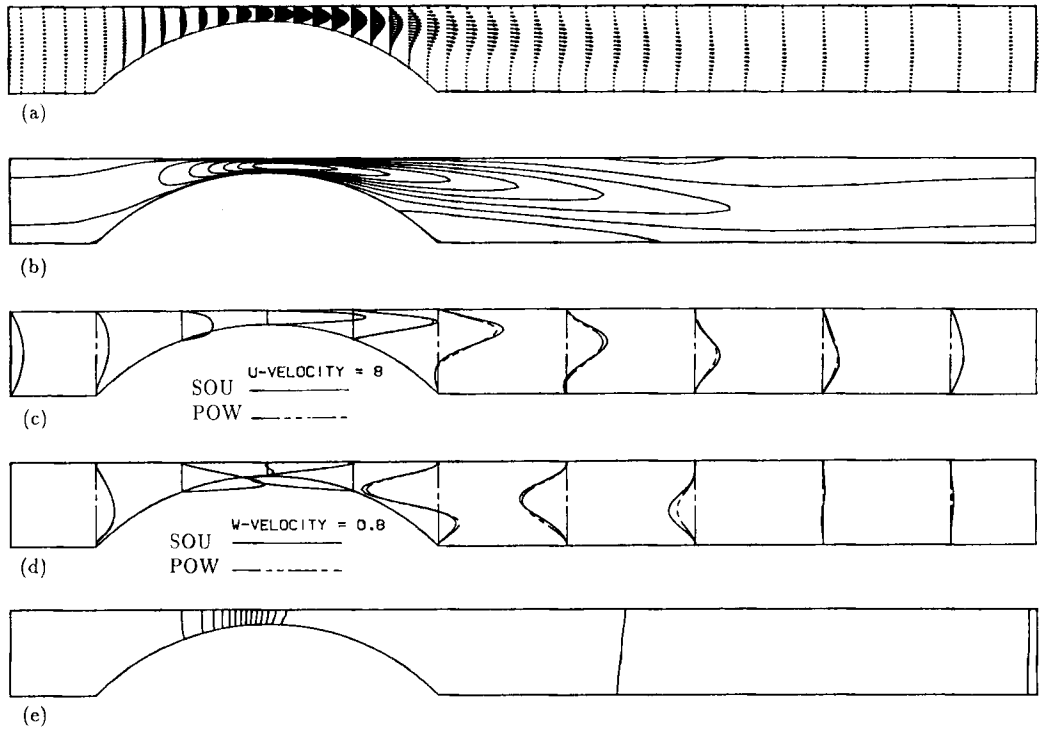

Figure 17. Flow in the symmetry plane at $Re = 50$, model M5: (a) velocity vectors; (b) U-velocity isolines; (c) U-velocity profiles; (d) W-velocity profiles; (e) isobars. The profiles are at positions $X = -6, -4, -2, 0, 2, 4, 7, 10, 13, 16$

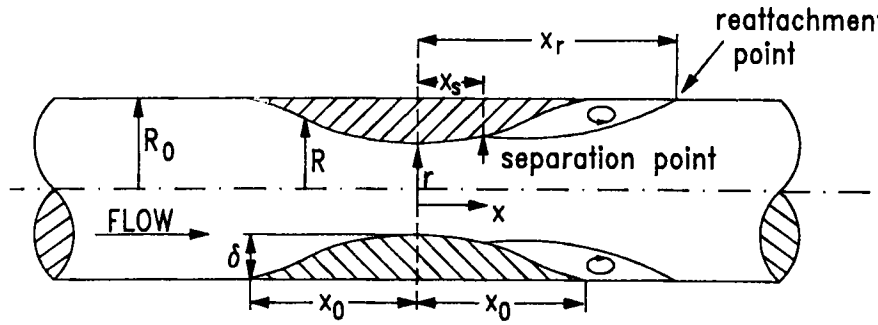

Figure 18. Geometric configuration for the axisymmetric constriction

Table VI. Model geometry

δ/R_0	x_0/R_0	Percentage reduction in flow area
1/2	2	75

$-4R_0$ to $14R_0$. Because of our earlier experience with calculations of laminar flow through constricted tubes, a 52×22 grid is selected. An initial calculation of the turbulent flow with a 42×12 grid indicates little change in the recirculation zone compared to the result from the 52×22 grid. Hence, further grid refinement seems unnecessary. The present grid is generated by transfinite interpolation (Figure 19). At the inlet, the grid point closest to the wall is outside the viscous sublayer.

At the inflow, $x = -4R_0$, the experimental data given by Deshpande and Giddens[13] are prescribed. They state that the u-velocity profile is in reasonable agreement with the fully developed power law profile ($n \cong 6{\cdot}4$) for $Re = 15\,000$. Hence, the velocity at the inflow is given by[14]

$$u = u_0\left(1 - \frac{y}{R_0}\right)^{1/6{\cdot}4}, \qquad v = 0 \tag{51}$$

where u_0 is the centreline velocity.

From the measurements of Deshpande and Giddens[13] only the velocity fluctuations u'_{rms} and w'_{rms} are given. When turbulent kinetic energy, k, at the inlet is estimated, it is assumed that v'_{rms} is equal to w'_{rms}. The dissipation rate of turbulent kinetic energy, ε, is estimated from[15]

$$\varepsilon = C_\mu^{3/4}\frac{k^{3/2}}{l}, \tag{52}$$

where $C_\mu = 0{\cdot}09$ and the length scale is given by

$$l = \min(0{\cdot}42\, y_{\text{wall}}, 0{\cdot}13\, R_0). \tag{53}$$

At the outflow boundary, the streamwise gradients are assumed zero.

In Table VII, the present calculated separation and reattachment lengths together with the measurements and the earlier calculations of Rastogi[16] and Kadja[15] are given. Whereas Rastogi

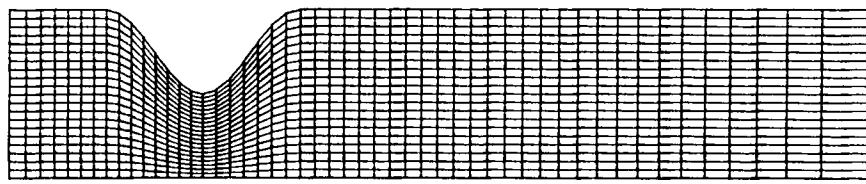

Figure 19. Grid for turbulent flow through an axisymmetric constriction

Table VII. Separation and reattachment lengths

	Separation, x_s/R_0	Reattachment, x_r/R_0
Experiment, Deshpande	$\approx 0{\cdot}4$–$0{\cdot}5$	4·0
Rastogi, 41×21, hybrid	1·2	2·4
Kadja, 44×32, POW	0·8	3·2
Kadja, 44×32, QUICK	0·8	3·5
Present, 52×22, POW	0·89	3·02
Present, 52×22, SOU	0·56	4·07

and Kadja used curvilinear orthogonal co-ordinates and a staggered grid arrangement, the present method is based on curvilinear non-orthogonal co-ordinates and a non-staggered grid arrangement. All calculations were based on the k–ε turbulence model together with wall functions.

The separation point was not measured, but the experimental velocity profiles indicate a separation point earlier than that predicted by SOU. SOU means that the momentum equations are solved by SOU while POW is used for solving the k- and ε-equations, since POW cannot produce negative k and ε values. Even if the calculations with POW and the hybrid scheme are expected to give approximately the same result (Table VII), considerable disagreement exists between the results of Rastogi and Kadja. The present result using POW produces

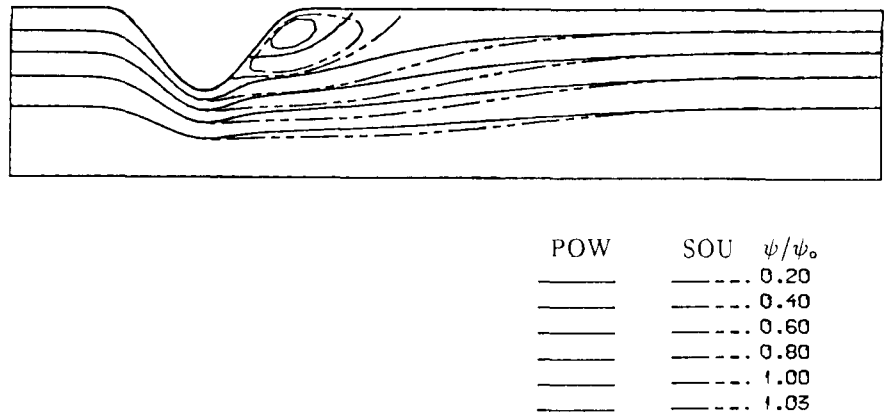

Figure 20. Streamlines

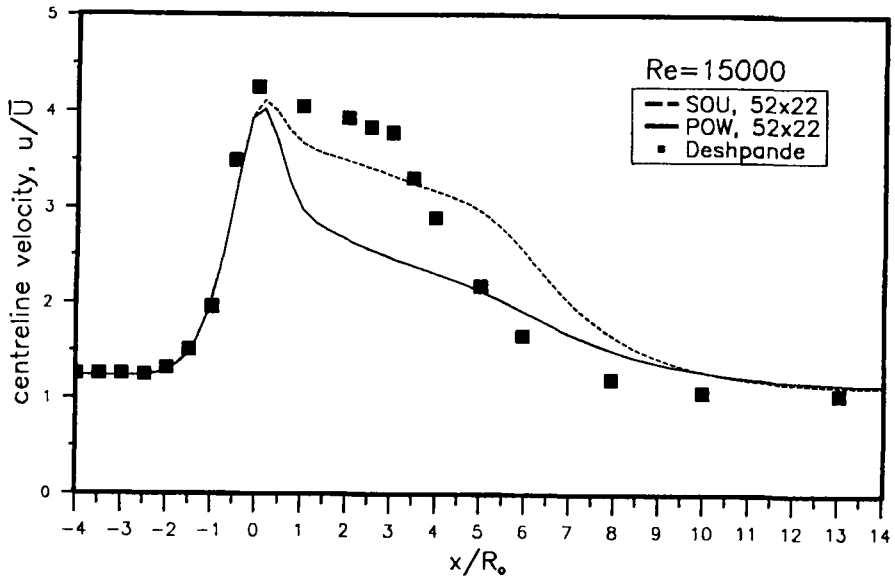

Figure 21. Centreline velocity

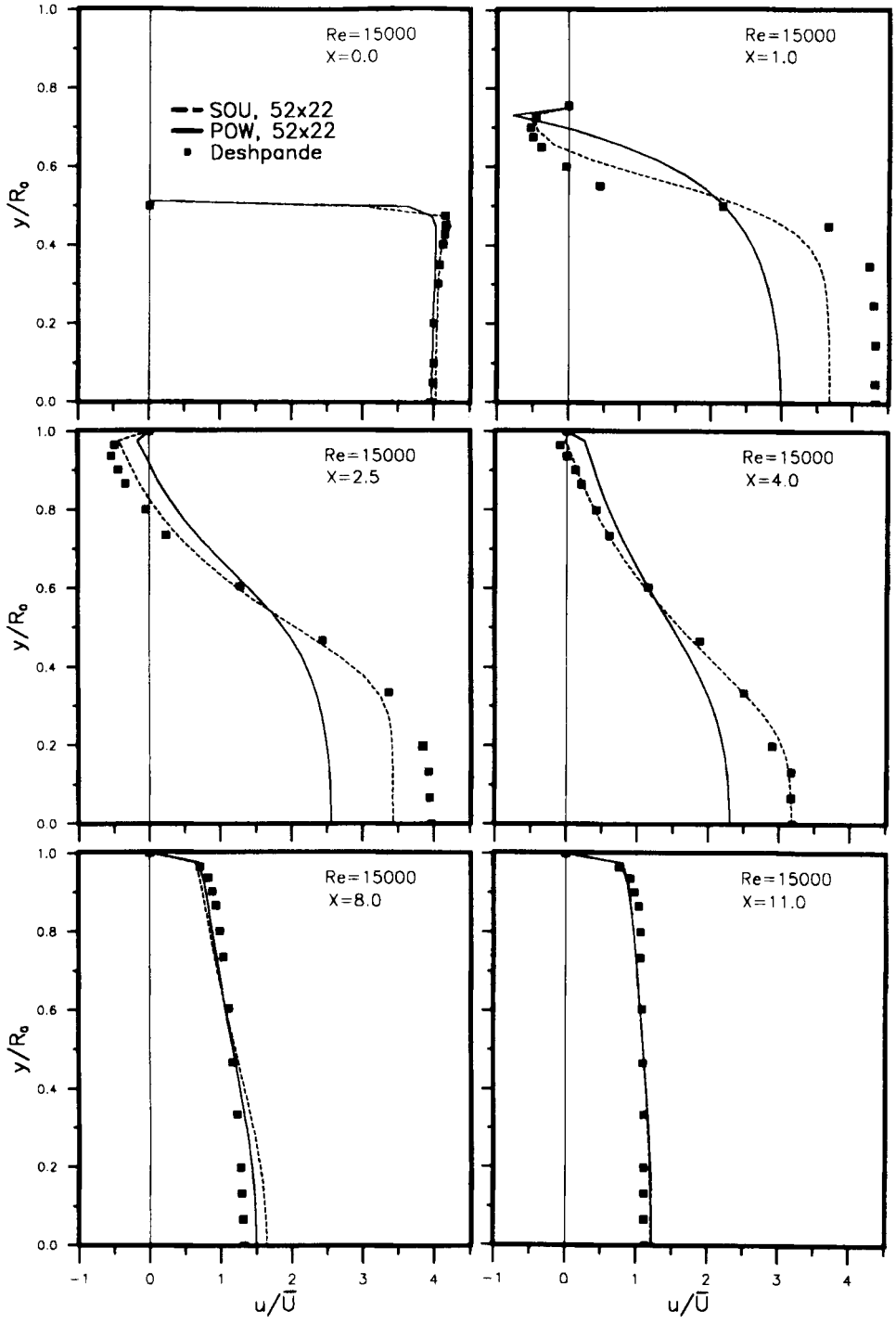

Figure 22. Axial velocity profiles at different x/R_0-positions

a smaller recirculation zone than that predicted by Kadja, but the agreement is satisfactory. When Kadja uses QUICK (Quadratic Upstream Interpolation for Convective Kinematics) instead of POW, a minor increase in the reattachment length appears. However, as the streamlines in Figure 20 indicate, the present calculation with SOU produces a much longer and thicker recirculation zone than POW. From Table VII it is evident that SOU gives a recirculation zone in close agreement with the measurements. Since SOU produces a more accurate recirculation zone than POW, the centreline velocity (Figure 21) and the u-velocity profiles at different x-positions (Figure 22) are also in closer agreement with the measurements.

The fluid is strongly accelerated in the converging part of the constriction, and afterwards deceleration takes place in the diverging part. Because of the severe adverse pressure gradients as the flow area increases, the flow separates from the curved wall. Both u-velocities (Figures 21 and 22) and the wall static pressures (Figure 23) are well predicted within the acceleration region. However, POW gives separation too late with a too early and excessive pressure recovery and a too early drop in the centreline velocity. Even if SOU gives a much better result, it is evident that the centreline velocity is not high enough in the recirculation region, and the velocity recovery occurs too late. Velocity profiles (Figure 22) indicate that the measured recirculation bubble is thicker than the one calculated by SOU. In Figure 22, the deviation between the calculated and the measured velocity profiles is greatest along the centreline. Since the flow is axisymmetric, small u-profile variations at the outer radial positions affecting mass flow continuity are supplemented by large adjustments near the axis.

In Figure 24, the predicted centreline turbulent kinetic energy is compared with measurements. The measured k is estimated from velocity fluctuations in the same way as at the inlet. Whereas the measured k increases considerably after separation occurs, the prediction indicates that k increases in two steps: first, in front of the constriction and, next, after the recirculation zone. Profile plots of k at different x-positions are shown in Figure 25. Downstream of the minimum area of the throat, SOU and POW predict different k-profiles.

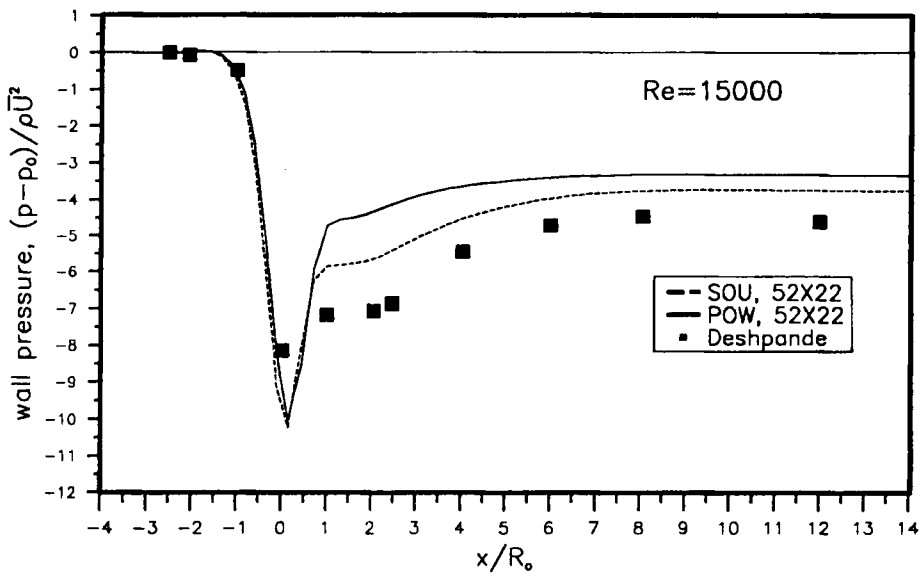

Figure 23. Wall static pressure

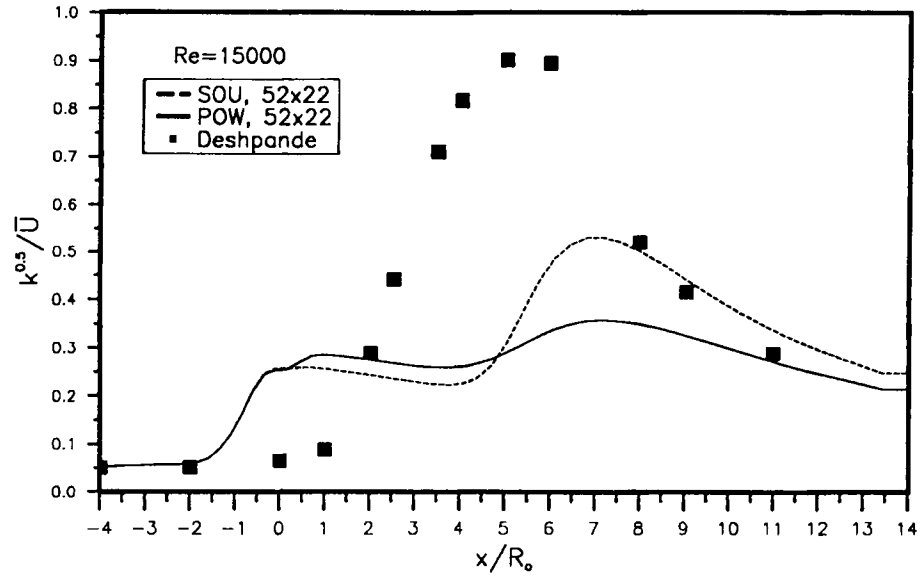

Figure 24. Turbulent kinetic energy profiles along the tube centreline

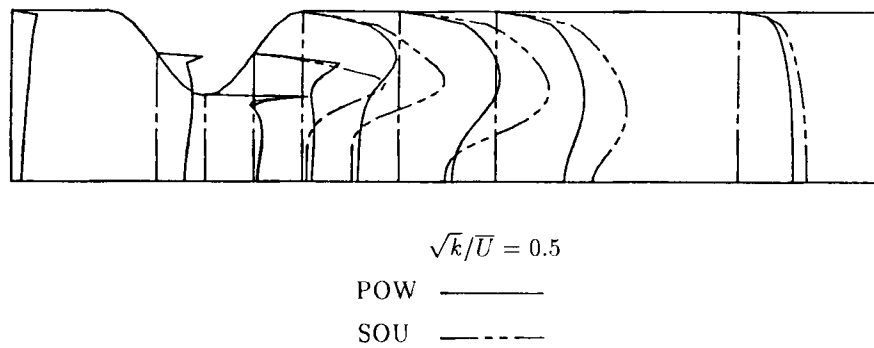

Figure 25. Turbulent kinetic energy profiles at different x-positions: $x/R_0 = -4, -1, 0, 1, 2, 4, 6, 11$

The present results indicate that SOU produces the best predictions of the flow. However, the agreement between the predicted and the measured turbulent kinetic energy is not satisfactory. But, if the present k-profiles are compared with the results by Kadja, the qualitative agreement seems good. In addition to the k–ε turbulence model, Kadja also tested an algebraic stress model. The change in the predicted turbulent kinetic energy along the centre line was small compared to the large deviation between prediction and measurement. Laminarization in the strongly accelerating wall-boundary layer, connected with an incomplete description of the near-wall dissipation during the deceleration process, were initially thought to be the main sources for the unsuccessful prediction. However, Kadja also calculated the flow with a low-Reynolds-number k–ε model without finding any noticeable improvement compared to the earlier calculations with wall functions. One of the changes obtained with the low-Reynolds-number k–ε model compared to

wall functions was the depression of the near-wall peaks of the turbulent kinetic energy in Figure 25. The reason for the disagreement is not well understood, but the stress transport in axisymmetric flow may be more important than what has been assumed until now.[17]

CONCLUSIONS

Laminar and turbulent two- and three-dimensional fluid flows inside constricted tubes and ducts with complex geometries are studied by a finite volume method based on curvilinear non-orthogonal co-ordinates (body-fitted co-ordinates) and a non-staggered grid arrangement. These complex geometries show the need for the high flexibility of the curvilinear non-orthogonal co-ordinates. The use of non-staggered grid arrangement simplifies the computer program system compared to a staggered grid arrangement. Later, the computer program system will be extended to a multiblock grid system so that the flexibility in describing complex geometries is even increased. This extension is simplified by a non-staggered grid arrangement. The turbulent flow is described by the high Reynolds number k–ε turbulence model together with wall functions. Generation of grids is achieved by transfinite interpolation and an elliptic grid generator.

The three-dimensional calculation of tube flow indicates that the treatment of the non-orthogonal terms is correct. When calculating the converging–diverging duct, the second-order upwind scheme is in better agreement with an earlier numerical result than the power law scheme. For the laminar flow through the non-axisymmetric constricted tubes, the second-order upwind scheme does not produce results that are in better accord with the experimental data than the power law scheme. However, this complex three-dimensional flow situation needs further grid refinement.

When turbulent flow through an axisymmetric constriction is calculated, the second-order upwind scheme produces results in better agreement with measurements than the power law scheme. Although the velocity and pressure are in satisfactory agreement with the measured values, the turbulent kinetic energy along the centreline is not in satisfactory accordance with the experimental data.

Curvilinear non-orthogonal co-ordinates together with a non-staggered grid arrangement are very useful in the analysis of flow inside complex geometries. The present results are believed to be within the accuracy of the turbulence model employed, and both the calculations of laminar and turbulent flows are in accordance with the earlier numerical results. The convergence properties of the algorithm are good.

ACKNOWLEDGEMENT

This study was supported by the Royal Norwegian Council for Scientific and Industrial Research (NTNF) and the National Program for Utilization of Natural Gas (SPUNG).

APPENDIX: NOMENCLATURE

$\mathbf{A}^{(i)}$	area vector
A^i_j	Cartesian area component
a_{nb}, a_P	coefficients in the discretized equation
b	source term in the discretized equation
$\mathbf{e}_{(i)}$, $\mathbf{e}^{(i)}$	covariant and contravariant basis vectors
$\mathbf{i}_k$	Cartesian unit vectors
$\mathbf{J}$	convective and diffusive flux vector

J	Jacobian determinant
J_i^j	Cartesian component of $\mathbf{e}_{(i)}$ $(=\partial x^j/\partial \xi^i)$
$\bar{J}_j^i$	Cartesian component of $\mathbf{e}^{(i)}$ $(=\partial \xi^i/\partial x^j)$
k	turbulent kinetic energy
nn	general indicator for the control volume faces; e, w, n, s, t, b
$\overline{\mathrm{Pe}}$	physical length between points P and e
p	pressure
$\mathbf{r}$	Cartesian position vector
S	source term
$\mathbf{U}$	velocity vector
U, V, W	non-dimensional velocities
u_i	Cartesian velocity components; u, v, w
V	volume
X, Y, Z	non-dimensional Cartesian co-ordinates
x_i	Cartesian co-ordinates; x, y, z
y_{wall}	distance from the wall

Greek characters

Γ	general diffusivity coefficient
δ	difference
δ_j^i	Kronecker delta
ε	dissipation rate of turbulent kinetic energy
μ	dynamic viscosity
ξ^i	curvilinear non-orthogonal co-ordinates; $\xi^1=\xi$, $\xi^2=\eta$, $\xi^3=\zeta$
ρ	density
φ	general dependent variable
ψ	stream function; ψ_0 is the maximum stream function difference at the inlet

REFERENCES

1. S. V. Patankar, *Numerical Heat Transfer and Fluid Flow*, McGraw-Hill, New York, 1980.
2. M. C. Melaaen, 'Analysis of curvilinear non-orthogonal coordinates for numerical calculation of fluid flow in complex geometries', *Ph.D. Thesis*, University of Trondheim, Norway, 1990.
3. M. C. Melaaen, 'Calculation of fluid flows with staggered and nonstaggered curvilinear nonorthogonal grids—the theory', *Numer. Heat Transfer*, Part B, **21**, 1–19 (1992).
4. M. C. Melaaen, 'Calculation of fluid flows with staggered and nonstaggered curvilinear nonorthogonal grids—a comparison', *Numer. Heat Transfer, Part B*, **21**, 21–39 (1992).
5. C.-M. Rhie and W. L. Chow, 'Numerical study of the turbulent flow past an airfoil with trailing edge separation', *AIAA J.*, **21**, 1525–1532 (1983).
6. M. Peric, 'A finite volume method for the prediction of three-dimensional fluid flow in complex ducts', *Ph.D. Thesis*, University of London, Imperial College, 1985.
7. A. D. Burns and N. S. Wilkes, 'A finite difference method for the computation of fluid flows in complex three dimensional geometries', *AERE-R 12342*, Harwell Laboratory, July 1987.
8. J. F. Thompson, Z. U. A. Warsi and C. W. Mastin, *Numerical Grid Generation, Foundations and Applications*, Elsevier, New York, 1985.
9. K. Miki and T. Takagi, 'A domain decomposition and overlapping method for the generation of three-dimensional boundary-fitted coordinate systems', *J. Comput. Phys.*, **53**, 319–330 (1984).
10. C. R. Maliska and G. D. Raithby, 'A method for computing three dimensional flows using non-orthogonal boundary-fitted co-ordinates', *Int. j. numer. methods fluids*, **4**, 519–537 (1984).
11. D. F. Young and F. Y. Tsai, 'Flow characteristics in models of arterial stenoses—I. Steady flow', *J. Biomech.*, **6**, 395–410 (1973).
12. A. K. Rastogi, 'Numerical calculation of fluid flow, heat and mass transfer in three-dimensional irregular domains', *A. S. Veritas Research Report No. 86-2028*, Norway, 1986.

13. M. D. Deshpande and D. P. Giddens, 'Turbulence measurements in a constricted tube', *J. Fluid Mech.*, Part 1, **97**, 65–89 (1980).
14. H. Schlichting, *Boundary-Layer Theory*, 7th edition, McGraw-Hill, New York, 1979.
15. M. Kadja, 'Computation of recirculating flow in complex domains with algebraic Reynolds stress closure and body fitted meshes' *Ph.D. Thesis*, University of Manchester, 1987.
16. A. K. Rastogi, 'Hydrodynamics in tubes perturbed by curvilinear obstructions', *Trans. ASME*, **106**, 262–269 (September 1984).
17. M. A. Leschziner, 'Numerical implementation and performance of Reynold-stress closures in finite-volume computations of recirculating and strongly swirling flows', Lecture Series 1987-06, von Karman Institute for Fluid Dynamics, 18–20 May 1987.